ARMA 14-7626

A micromechanical analysis on permeability evolutions of a dilatant shear band

Sun, WaiChing
Department of Civil Engineering and Engineering Mechanics, Columbia University, New York, NY10027, USA
Kuhn, Matthew R.
Donald P. Shiley School of Engineering, University of Portland, Portland, OR97203, USA
Rudnicki, John W.
Department of Civil and Environmental Engineering, Northwestern University, Evanston, IL60208, USA

This paper was prepared for presentation at the 48th US Rock Mechanics / Geomechanics Symposium held in Minneapolis, MN, USA, 1-4 June 2014.

ABSTRACT: This paper presents a multi-scale lattice Boltzmann/finite element scheme that quantitatively links particulate mechanics to hydraulic properties of a grain assembly obtained from a simple shear discrete element simulation. A spatial homogenization is performed to recover the macroscopic stress from the micro-mechanical force chances. The pore geometries of the shear band and host matrix are then quantitatively evaluated through morphology analysis and flow simulations. Hydraulic properties estimated from multiscale flow simulations are compared with those inferred from volume averaging and geometric averaging schemes. Results from the discrete element simulations imply that grain sliding and rotation occur predominately within the dilatant shear band. These granular motions lead to dilation of pore space inside the shear band and increases in local permeability. While considerable anisotropy in the contact fabric is observed within the shear band, anisotropy of the permeability is, at most, modest in the assemblies composed of spherical grains.

1. INTRODUCTION

Deformation bands in geological materials refer to narrow zones of inhomogeneous strain. Their development is often analyzed as a material bifurcation phenomenon that takes place as an alternative to homogeneous deformation (Rudnicki & Rice 1975). Deformation bands can be categorized as shear, compaction, or dilation, depending on the predominant mode of localized strain within the band. In geological materials, shear occurs most commonly with some amount of volumetric deformation, either dilation or compaction (Rudnicki, 2004; Aydin et al. 2006; Sun et al. 2011b). A dilatant shear band can cause an increase in porosity and change of flow path, thereby altering the fluid transport inside the pore space. This feature is of economic importance, because dilatant shear bands may act as flow conduits that leak injected pore-fluid in reservoirs (Wawersik et al. 2006).

To predict how formation of dilatant shear bands affects hydraulic properties, in particular, permeability, macroscopic finite element analysis can be used to capture the evolution of porosity. Changes of permeability are then estimated from the porosity evolution via Kozeny-Carman or other empirical relations. This macroscopic approach, however, cannot provide information on how microstructural attributes, such as grain sliding, rotation and rearrangement, affect hydraulic properties. Furthermore, a macroscopic empirical porosity-permeability relation may fail to deliver reliable prediction when the permeability changes are caused by factors other than volumetric changes of pore space, such as isolation of the pores and changes in tortuosity and size distribution of flow channels as shown in Sun et al. 2011a. Volumetric digital image correlation applied to X-ray tomography images of geomaterials can help understanding the kinematics of grains motion and changes in pore geometry as shown in Lenoir et al. 2007. However, due to the technical difficulty of conducting mechanical tests while simultaneously performing CT X-ray imaging, experimental measurement of microstructural attributes is rare (e.g., Hall et al. 2010).

To analyze the links between microstructural granular motion and macroscopic hydraulic properties in a repeatable and cost-efficient way, we introduce a multiscale numerical alternative. This approach incorporates the discrete element method to simulate grain motion inside the dilatant shear band and a

multiscale lattice Boltzmann/finite element scheme to capture the evolution of permeability. Since the motion of every particle in the DEM ensemble is recorded at every time step, this approach makes it possible to quantify how individual particles affect pore geometry and macroscopic hydraulic properties without the need to introduce an additional phenomenological law.

This work is an extension of the research reported previously in Sun, et al. 2013. For completeness, part of the results previously reported in Sun et al. 2013 will be mentioned.

2. METHOD

In this study, we use the open source 3D discrete element code OVAL to simulate a dry simple shear test on a specimen composed of spherical particles (Cundall & Strak 1979; Antonellini & Pollard 1995; Iwashita & Oda 1998; Iwashita & Oda 2000, Kuhn, 2004; Wang et al. 2008). We then analyze how formation of a shear band changes the microstructural attributes of the granular materials using a variety of tools, including a hybrid lattice Boltzmann-finite element simulations, and network measures from graph theory, such as the Euler-Poincare characteristics and the Cheeger constant. The goal is to understand how plastic dilatancy caused by grain rearrangement affects the hydraulic characteristics of both the host matrix and the shear band, before and after the formation of dilatant shear band.

2.1 Grain assembly from discrete element simulations

A three-dimensional discrete element simulation is conducted via a DEM code OVAL (Kuhn, 2004, 2011). The grain assembly consists of spherical particles, among which simplified constitutive contact laws explicitly model the grain-to-grain interactions. The motion of each particle is obtained through force and momentum balances that read,

$$\begin{aligned} m\ddot{u} + C^m\dot{u} + P(u) &= F_{ext} \\ I\ddot{\omega} &= M_{ext} \end{aligned} \tag{1}$$

where m and C^m are the mass and translational damping. $P(u)$ is the net force imbalance vector due to the inter-grain contact forces and F_{ext} denotes the external loads exerted by the walls or gravity. I is the moment of inertia and $\ddot{\omega}$ is the rotational acceleration and M_{ext} is the external moment acting on the particular grain. The governing equations listed in (1) are solved via a explicit central difference time integrator. Introducing mass Cm into the balance laws and contact dampings Cs in the grain contact constitutive model approximates the quasi-static condition.

In our implementation, we use a simplified contact model in which the grain-to-grain force-displacement relation is governing by a frictional Hertz-Mindlin mechanism with viscous contact damping. Since our goal is to simulate the granular nature of cohesion-less material, no force due to cohesive bonding is assigned. The resultant constitutive law reads,

$$\begin{aligned} df^n &= k^n d\delta;\ k^n = \frac{\sqrt{2}G_g\sqrt{R^e}}{1-\nu}\ \delta^{1/2} \\ df^t &= k^s ds;\ \ k^s = \frac{2\sqrt{2}G_g\sqrt{R^e}}{2-\nu}\ \delta^{1/2} \end{aligned} \tag{2}$$

where δ is the indentation at the contact, G_g and ν is the shear modulus and Poisson ratio of the grains and R^e is the effective radius, which is the a function of the radii of two contacted grains R_1 and R_2, i.e.,

$$R^e = \frac{2R_1R_2}{R_1+R_2} \tag{3}$$

In addition, the tangential force is limited by the frictional coefficient such that,

$$|f^t| \le \mu^f f^n \tag{4}$$

where μ^f is the frictional coefficient. To maintain quasi-static simulation, a viscous damping force is applied at each contact, i.e.,

$$f^{vis} = C^s\dot{s} \tag{5}$$

where $\dot{s}$ is the tangential sliding velocity at a contact. This contact viscosity is diminished when the frictional sliding occurs, as such sliding becomes a dissipation mechanism that prevents spurious grain vibrations. The DEM simulation was conducted with an assembly of 129000 spherical grains that were densely arranged with an initial isotropic fabric. The assembly has a grain size distribution of a poorly graded sand, with a coefficient of uniformity C_u of 1.4, and the median particle diameter of 10mm. The dense arrangement was attained from an initially sparse random arrangement of particles by isotropically reducing the boundary dimensions. During the isotropic compaction phase, the frictional force was temporarily removed. This technique was previously used in Thornton, 2000. The porosity of the compacted assembly is 0.337.

2.2 Multi-scale hybrid LBM-FEM simulations

To overcome the computational constraint on the size of numerical specimens and estimate effective permeability in a cost-efficient way, we implement the multi-scale finite element/Lattice Boltzmann method proposed by White et al (White et al 2006) and employ it on a 3D reconstructed image of Aztec sandstone from the Valley

of Fire State park (Lenoir et al 2010). The calculation of macroscopic effective permeability of the specimen involves only three simple steps.

First, the entire specimen is divided into cubic unit cells of identical sizes in which the local effective permeability is measured. Providing that these unit cells are large enough to contain sufficient information about the microstructure but small enough to preserve the macroscopic heterogeneity (Giltman et al. 2007), then one can recover the local effective permeability of the unit cell through lattice Boltzmann simulations.

The lattice Boltzmann simulations are conducted in each unit cell with the following governing equation i.e.,

$$\frac{\partial f_i}{\partial t} + e_i \cdot \frac{\partial f}{\partial x} = C_i \qquad \text{in } \Omega^c \tag{7}$$

where f_i and e_i are the distribution function and the lattice microscopic velocity respectively. Ω_c denotes the spatial domain of the unit cells. The evolution of the distribution function depends on how fluid molecules collide with each others. This interaction is replicated by the collision operator C_i.

By assuming that the permeability tensor is symmetric, the six independent components of the locally homogenized effective permeability tensor k_{ij} can be computed by applying different boundary conditions on the same numerical specimen. By relating volume averaged velocity $<v_i(x)>$ with the prescribed macroscopic pressure gradient p,j, the local effective permeability k_{ij} can be recovered via the Darcy's law, i.e.,

$$k_{ij} = - < v_i(x) > \frac{\mu}{p_{,j}} \tag{8}$$

where μ is the kinematic viscosity and <…> denotes the volume average over a local unit cell. The macroscopic velocity and pore pressure are defined in terms of the microscopic quantities f and e_i, i.e.,

$$p = c^2 \rho; \quad \rho = \sum_{i=1}^{\alpha} f_i$$

$$v_a = \sum_{i=1}^{\alpha} f_i e_{ia} \Big/ \sum_{j=1}^{\alpha} f_j \tag{9}$$

where a denotes the number of possible collision direction of the lattices and c denotes the speed of the sound which is treated as a constant in lattice Boltzmann simulations (Succi 2001). Finally, the overall effective permeability of the specimen is computed by solving the macroscopic incompressible pore-fluid transport problem with neglected body forces via finite element method, i.e.,

$$\begin{aligned} v_{j,j} &= 0 && \text{in } \Omega^s \quad \text{(continuity equation)} \\ v_i &= -\frac{k_{ij}}{\mu} p_{,j} && \text{in } \Omega^s \quad \text{(Darcy's law)} \end{aligned} \tag{10}$$

where Ωs is the spatial domain of the numerical specimen. In the macroscopic finite element problem, the local effective permeability k_{ij} is assumed to be uniform inside each unit cell and the overall effective permeability is computed by applying equation (1) to the specimen domain, as shown in Figure 1.

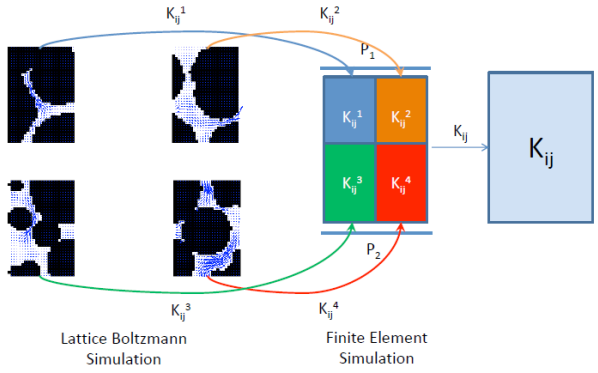

Fig. 1. Multiscale numerical scheme used to determine effective permeability in large scale. Reproduced from Sun, et al. 2011a.

2.3 Geometrical Analysis on void space in simulated assembly

When a deformation band forms, the plastic deformation would concentrate in a narrow zone. In the DEM simulations presented in this paper, we did not introduce any constitutive law or mechanism to simulate grain crushing. As a result, this concentration of plastic deformation is mainly due to the grain rotation and re-arrangement inside the shear band. In such case, one can view the contact network as a mathematical object called a contact graph, and thus one can measure how the topology of the contact network and pore space time inside and outside the deformation band change over time using measures made available from graph theory (Tordesillas, 2007, 2010; Tordesillas & Muthuswamy, 2009; Sun et al 2011a; Sun et al 2011b; Sun et al., 2013).

Here we introduce the usage of two common numerical measures from graph theory to measure the geometrical attributes of both the pore space and solid contacts, inside and outside the shear band. For the pore space problem, we first generate an binary image of DEM assemblies using the region growing method outlined in Sun et al. 2011a and Sun et al. 2013, then assign vertex on each void voxel and connect each pair of neighbor vertices with edges to form an connected graph. We then compute the Euler-Poincaré characteristic of flow network, which reads,

$$\mathrm{E} = N - C + H \tag{11}$$

where E is the Euler number, N is the number of interconnected pores, C is the number of loops in the pore space and H is the number of objects completed enclosed by pore space. As a result, the Euler-Poincaré characteristic measures how "connected" the pore space is. A positive Euler-Poincaré characteristic indicates less branching in the flow path, while a negative one indicates an interconnected, network-like pore geometry.

The second numerical measure we use is the Cheeger constant (Chung, 1997). We compute the Cheeger constant on the solid grain contact network. The solid network is formed by assigning vertex to represent each grain and forming edges to represent the contacts of pairs of contacted grains. The topology of the grain assembly is therefore represented by an undirected finite graph composed of vertices (representing the grains) connected by edges (representing the normal contact).

Now, let G be the entire undirected finite graph with vertex set $V(G)$ and edge set $E(G)$. Let A be a subset of V(G), i.e., a collection of grains in the assembles, and that ∂A be all the edges connecting A to neighboring vertices outside of A, i.e.,

$$\partial A = \{(x,y) \in E(G) \mid x \in A, y \in V(G) \setminus A\} \qquad (12)$$

The Cheeger constant, which denoted as $h(G)$ herein, is defined as,

$$h(G) = \min\{\frac{|\partial A|}{|A|} : A \subseteq V(G), 0 < |A| < \frac{|V(G)|}{2}\} \qquad (13)$$

where $|A|$ and $|\partial A|$ are the number of grains and grain contacts in the subset A. In other words, the Cheeger constant measures how easy or difficult the grain assemblies can be cut into two pieces with no contact in between. A low Cheeger constant indicates that such a cut reduces a fewer number of contacts, while a high Cheeger constant indicates a more robust contact network. Here our goal is to use Cheeger constant to quantify changes in microstructural attributes due to rearrangement and rotation of grains inside the shear band affecting force distribution in the grain assemblies.

3. RESULTS

We study the geometrical attributes inside and outside a dilatant shear band formed during a simple shear test simulations at 12% shear strain, and compare it with the permeability calculation to determine how changes of pore geometry affect the hydraulic properties. Figure 2 shows the rotation magnitude (in radians) of the grains in the assembly subjected to simple shear loading before and after the formation of a dilatant shear band. One interesting characteristics we observed is that grain rotations are mostly concentrated inside the shear band.

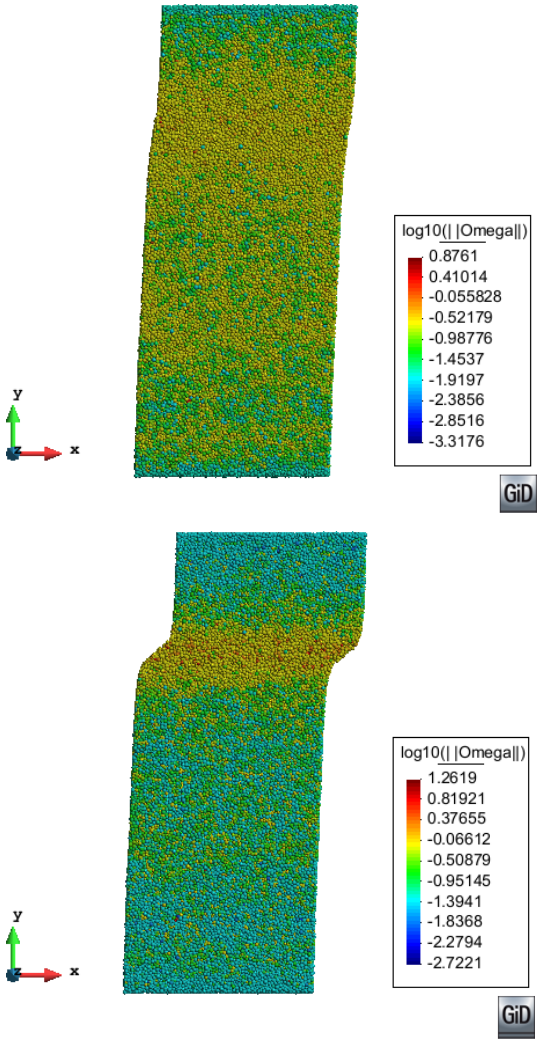

Fig. 2. Spatial distribution of rotation magnitude in assembly at shear strain = 6%(top) and 12% (bottom). Figure reproduced from Sun et al. 2013.

We also analyzed the pore geometry of 18 unit cells in the sizes of 4mm X 4mm X 4mm: nine inside the shear band and nine outside the shear band. We found that the averaged Euler-Poincaré characteristic of the pore space changes from -491 to -360 (a 26% decrease), while the host matrix counterpart changes from -438 to -493 (a 12% increase) as shear strain monotonically increases from 0 to 12%. This trend is consistent with the more significant porosity increase of the shear band (from 0.33 to 0.38), and the nearly constant porosity observed in the host matrix (from 0.32 to 0.33).

This change in the pore space topology is due to the rearrangement of grains due to rotation as observed in Figure 1. To further analyze how grain arrangement affects the pore geometry, we compute an approximated Cheeger constant for the grain cluster at shear strain = 12%. The procedure is as followed. First, we sampled a regions of the assembly both inside and outside the shear band. The sizes of the sample regions ranged from $1mm^3$ to $512mm^3$. For each given size, we then selected 400 samples (200 inside and 200 outside the shear band) and

counted the number of particles for each sample, as well as the number of solid contacts that can cut the sample from the assembly. The results are shown in Figure 3. We found that the approximated Cheeger constant is both less than one inside and outside the shear band. Nevertheless, the Cheeger quotient seems to be consistently lower inside the shear band. This small difference indicates that the grain contact network is slightly easier to form force bottlenecks than that of the host matrix. This tendency however is not insignificant and thus the contact networks inside the shear band and host matrix are more or less similar, even though the porosity is different.

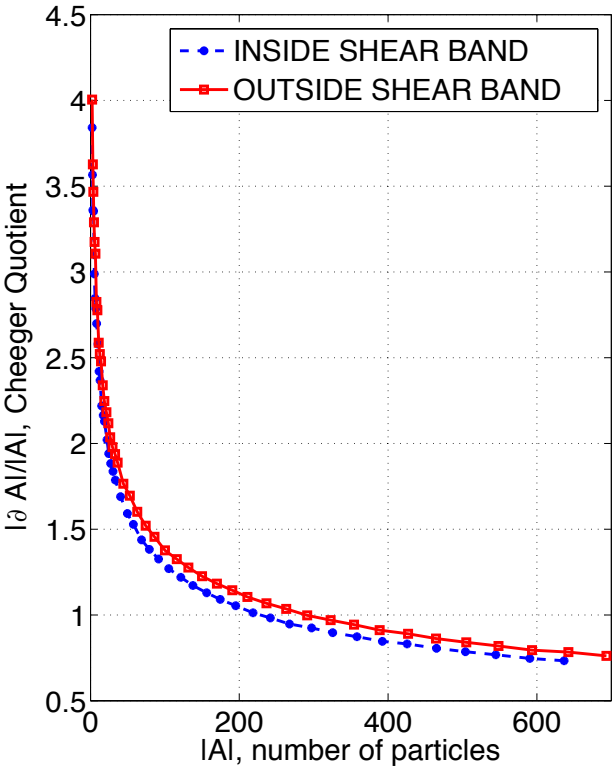

Fig. 3. Cheeger Quotient vs. number of particles for grain assembles inside (blue) and outside (red) the shear band at shear strain =12%.

Figure 4 presents the computed streamlines of a unit cell obtained from lattice Boltzmann simulations when shear strain = 12%. While prescribed by the same amount of pore pressure, the flow velocity inside the shear band is found to be, on average, higher than that of a host matrix. The multiscale FEM-LBM computation reveals that the permeabilities in normal and parallel directions of the shear band are 900 and 823 Darcy inside the shear band. Meanwhile, the permeabilities in the norm and parallel direction of the shear band are 480 and 460 Darcy in the host matrix. This difference is consistent with the 5% difference in porosity inside and outside the shear band. The changes in the Euler number also indicates that the pore space is less network-like inside the shear band, presumably due to the increase in pore pressure. Nevertheless, we do not observe any bottleneck among the solid contacts of the assembly, inside or outside the shear band.

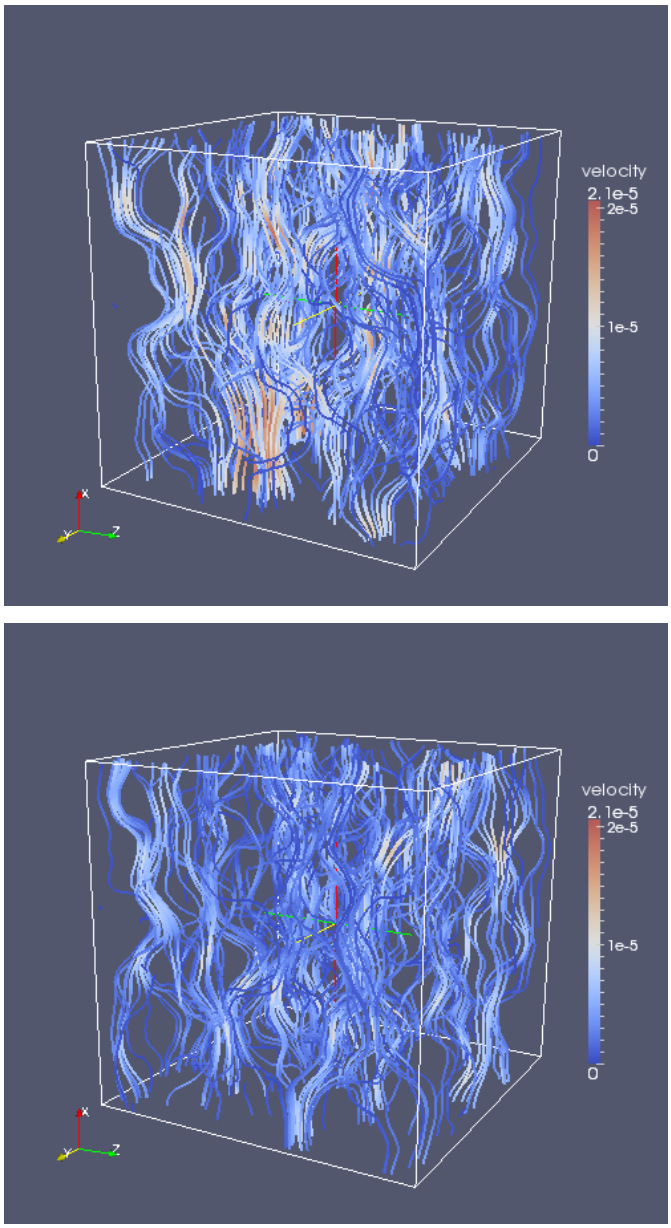

Fig. 4. Streamline in pore space inside (top) and outside (bottom) the shear band at shear strain =12%.

CONCLUSION

We present the usage of metric from graph theory to measure the topology of both the solid contact network and pore space and establish links to explain how differences of the connectivity of solid grains and pore space may affect the permeability.

REFERENCES

1. Bardet, J.P. (1994), Observations on the effects of particle rotations on the failure of idealized granular materials, *Mechanics of Materials*, **18**, 159-182.

2. Chung, F.R.K. Spectral graph theory. Vol. 92. *American Mathematical Soc*., 1997.

3. Cundall, P.A. and O.D.L. Strack. 1979. A discrete numerical model for granular assemblies, *Géotechnique* **29**(1):47–65.

4. Hall, S., M. Bornert, J. Desrues , Y. Pannier, N. Lenoir, G. Viggiani and P. Besuelle. 2010. Discrete and continuum analysis of localized deformation in sand using X-ray CT and volumetric digital image correlation, *Géotechnique*, **60**(5):315-322.

5. Iwashita K and M. Oda. 1998. Rolling Resistance at Contacts in Simulation of Shear Band Development by DEM. *Journal of Engineering Mechanics,* **124**:285-92.

6. Iwashita K and M. Oda. 2000. Micro-deformation mechanism of shear banding process based on modified distinct element method, *Powder Technology,* **109**:192-205.

7. Kuhn, M.R. and K. Bagi. 2004. Contact rolling and deformation in granular media, *International Journal of Solids and Structures*, **41**, No.21, 5793-5820.

8. Kuhn, M.R. 2011, Transient rolling friction model for discrete element simulations of sphere assemblies, in review.

9. Lenoir, N., J.E. Andrade , W.C. Sun, and J.W. Rudnicki. 2010. Permeability measurements in sandstones using X-ray CT and lattice Boltzmann calculations inside and outside of compaction bands, *Advances in Computed Tomography for Geomaterials*, GEOX2010, ISTE & Wiley, 279-286.

10. J.W. Rudnicki J.W. and J.R. Rice. 1975. Conditions for the Localization of Deformation in Pressure-Sensitive Dilatant Materials", *Journal of the Mechanics and Physics of Solids* **23**:371-394.

11. M. Ode and K. Iwashita. 2000. Study on coupled stress and shear band development in granular media based on numerical simulation analysis, *International Journal of Engineering Science* **38**:1713-1740.

12. R. Salgado and P. Bandini. 2000. Shear strength and stiffness of silty sand, *Journal of Geotechnical and Geoenvironmental Engineering*, 126(5):451-462.

13. Sun, W.C., J.E. Andrade, J.W. Rudnicki. 2011a. Multiscale method for characterization of porous microstructures and their impact on macroscopic effective permeability, *International Journal of Numerical Methods in Engineering* **88***(*12):1260-1279.

14. Sun, W.C., J.E. Andrade, J.W. Rudnicki and P Eichhubl. 2011b. Connecting microstructural attributes and permeability from 3D tomographic images of in situ shear-enhanced compaction bands using multiscale computations, *Geophysical Research Letter* **38**, L10302.

15. Sun, W.C., M.R. Kuhn, and J.W. Rudnicki. 2013 "A multiscale DEM-LBM analysis on permeability evolutions inside a dilatant shear band." *Acta Geotechnica* 8(5)465-480.

16. Tordesillas, A. 2007. Force chain buckling, unjamming transitions and shear banding in dense granular assemblies. Philosophical Magazine, 87(32):4987-5016.

17. Tordesillas, A. and M. Muthuswamy. 2009. "On the modeling of confined buckling of force chains." Journal of the Mechanics and Physics of Solids 57.4:706-727.

18. Tordesillas, A., D.M. Walker, and Q. Lin. "Force cycles and force chains." *Physical Review E* 81.1 (2010): 011302.

19. Wang, B., Y. Chen, T-f Wong. 2008. A discrete element model for the development of compaction localization in granular rock, *Journal of Geophysical Research*, 113, B03202.

20. Wawersik, W.R. et al. 2001. Terrestrial sequestration of CO_2: an assessment of research needs, *Advances in Geophysics*, **43**, 97-117.

21. White J.A., R.I. Borja and J.T. Fredrich. 2006. Calculating the effective permeability of sandstone with multiscale lattice Boltzmann/finite element simulations, *Acta Geotechnica* **1** 195-209.

22. Zhan, X., L.M. Schwartz, M.N. Toksoz, W.C. Smith, and F.D. Morgan. 2010. Pore-scale modeling of electrical and fluid transport in Berea sandstone, *Geophysics*, 75(5):135-142.